geosciences

MDPI

Article

The Sequence Stratigraphic Division and Geological Significance of Lower-Middle Ordovician Carbonate Rocks in Fuman Area, Tarim Basin, China

Hongyu Xu [1,2], Xi Zhang [1,2,*], Zhou Xie [3], Chong Sun [3], Pingzhou Shi [3], Ruidong Liu [3], Lubiao Gao [1,2], Jinyu Luo [1,2] and Tenghui Lu [1,2]

[1] School of Geoscience and Technology, Southwest Petroleum University, Chengdu 610500, China; 15319729548@163.com (H.X.)
[2] Sichuan Key Laboratory of Natural Gas Geology, Southwest Petroleum University, Chengdu 610500, China
[3] Research Institute of Exploration and Development, Tarim Oilfield Company, Petrochina, Korla 841000, China
* Correspondence: zhangx@swpu.edu.cn

Abstract

Oil and gas exploration conducted in the main fault zone of the Fuman Oilfield has yielded large-scale and high-production results. Against this background, the non-fault zone has emerged as a new domain for oil exploration endeavors. Nevertheless, the establishment of a unified sequence division scheme for the study area remains unachieved, primarily constrained by two key factors: first, the high costs associated with ultra-deep high-density coring operations; and second, the inconspicuous response characteristics exhibited by logging curves. This absence of a standardized scheme has further impeded the progress of oil and gas exploration in the non-main fault inter-region within the study area. Consequently, the present study is based on multi-source data, including seismic data, logging data, and field outcrop data. Magnetic susceptibility measurements from the cement plant section and natural gamma-ray logging data from the Yangjikan section were systematically analyzed to establish cyclostratigraphic frameworks. A sedimentary noise model (SNM) was employed to reconstruct Holocene sea-level fluctuations, enabling precise sequence stratigraphic subdivision within the Fuman Area. Results demonstrate that the Middle-Lower Ordovician Yijianfang–Penglaiba Formations retain robust astronomical cyclicity, validated by high-fidelity orbital forcing signals. Notably, the DYNOT (Dynamic Noise After Orbital Tuning) model effectively decouples orbital-driven sea-level oscillations from local depositional noise, offering a novel approach for sequence boundary identification. This methodology reveals a hierarchical sequence architecture comprising four third-order sequences and 11 fourth-order sequences within the Yijianfang–Penglaiba Formations. Such a framework provides critical insights into facies distribution patterns and non-fault-controlled exploration potential in the Fuman Basin.

Keywords: Fuman Area; Lower-Middle Ordovician; sequence stratigraphy; cyclostratigraphy; sedimentary noise model

Check for updates

Academic Editor: Michele Morsilli

Received: 17 November 2025
Revised: 3 March 2026
Accepted: 5 March 2026
Published: 25 March 2026

Copyright: © 2026 by the authors. Licensee MDPI, Basel, Switzerland. This article is an open access article distributed under the terms and conditions of the Creative Commons Attribution (CC BY) license.

1. Introduction

The Tarim Basin hosts significant ultra-deep marine carbonate oil and gas resources. Recent exploration advancements beyond conventional "paleo-uplift-controlled oil accumulation and slope-zone hydrocarbon enrichment" paradigms, combined with innovations in seismic imaging, drilling systems, and enhanced recovery technologies, have led to

the identification of the Fuman Oilfield—a strike-slip fault-controlled hydrocarbon accumulation exceeding 7500 m in depth. This major breakthrough in the basin's depression zone holds proven geological reserves of 1 billion tons of oil equivalent (BOE), positioning it as a strategic target for developing fracture-vuggy carbonate reservoirs in ultra-deep settings [1]. While significant progress has been made in oil and gas exploration within primary strike-slip fault zones, identifying under-explored inter-fault regions has emerged as a strategic priority to sustain ultra-deep hydrocarbon reserves and production growth [2]. The major breakthrough in condensate gas exploration achieved by Well Fudong 1 within the intra-platform shoal of the Ordovician Yingshan Formation in the non-main fault zone has confirmed that the intra-platform shoal sedimentary zone situated between main faults constitutes a key exploration area endowed with oil and gas accumulation potential. Nevertheless, a systematic stratigraphic division scheme for the third-order and fourth-order sequences of the Ordovician in the Fuman Area has not yet been established. This limitation not only impedes the accurate identification and forecasting of favorable depositional facies critical for high-quality reservoir development but also obstructs systematic exploration strategies in non-main fault-controlled regions. Following Vail et al.'s (1987) theoretical framework of sequence stratigraphy, the current third- and fourth-order sequence stratigraphic frameworks in the Fuman Area present the following challenges [3]: 1. Limited seismic resolution restricts the division of fourth-order and higher-order sequence stratigraphy; 2. Ultra-deep coring is costly, resulting in insufficient core data; 3. The logging response characteristics of fourth-order and higher sequence stratigraphic boundaries are not obvious. In recent years, the development of cyclostratigraphy has provided new ideas for sequence stratigraphic division [4–7]. This study attempts to identify the astronomical orbital cycle parameter information in the strata based on logging data. Using the sedimentary noise model of orbital parameters [8], it reconstructs high-precision sea-level fluctuations to realize third-order and fourth-order sequence stratigraphic division. Additionally, the third-order and fourth-order sequences delineated based on field outcrop data are employed to validate this model and demonstrate its reliability. Should the reliability of this methodology be verified, it will enable the "high-efficiency and low-cost" division of third-order and fourth-order sequences that relies exclusively on logging data. This study will establish a solid scientific basis for characterizing favorable sedimentary facies and advancing oil–gas exploration in the region. To emphasize its novelty, we integrate insights on paleoenvironmental shifts in the Bohai Bay Basin, thereby reinforcing our contributions to regional geology, cyclostratigraphy, and sequence stratigraphic frameworks [9].

2. Geological Setting

The Tarim Basin, situated in southern Xinjiang Uygur Autonomous Region, China, is bounded by the Tianshan, Altun, and Kunlun mountain ranges. This composite basin, characterized by its superimposed tectonic architecture, represents a stable ancient craton within the Tarim Plate. Surrounding its periphery are multi-stage tectonic activity zones linked to plate-margin processes [10]. The Fuman Area lies within the northern depression, a secondary tectonic unit of the Tarim Basin. This study focuses on the Aman Transition Zone in the central northern depression (Figure 1A) [11]. The Aman Transition Zone is a transitional area between the Awati Sag and the Manjiaer Sag, bordering the Manjiaer Sag to the east, linking to the Tazhong Uplift (Central Uplift) to the south, adjoining the Awati Depression to the west, and grading into the Tabei Uplift to the north [12]. During the Late Cambrian to Early Ordovician period, the Tarim Basin was generally in an east–west-trending weak extensional stress environment. A large carbonate platform was formed in the western part of the Manjiaer Depression [13,14], with its tectonic–paleogeographic features characterized by higher terrain in the south and west and lower terrain in the north

and east. In the Middle Ordovician, the Tazhong area was gradually uplifted into a large fault uplift due to north–south compression [15], while a nearly east–west trending subaqueous low uplift was formed in the Tabei area. The overall structure was relatively gentle. The Aman area, located between the two, became part of the extension of the Tabei area and initially formed the prototype of the Aman Transition Zone. By the end of the Ordovician period, uplift persisted in the Tabei area, further accentuating the slope characteristics of its southern margin. Concurrently, the Manjiaer Sag evolved, and the Aman Transition Zone emerged [16]. During the Late Caledonian period, the Tabei Uplift experienced renewed uplift, enhancing and finalizing the south-dipping slope characteristics of the extensive Aman Transition Zone. In the Himalayan period, Mesozoic–Cenozoic strata in the Aman Transition Zone tilted northward, while Lower Paleozoic strata maintained a southward tilt. Subsequently, the current tectonic framework of the Aman Transition Zone was established (Figure 1B) [17]. The Fuman Area has an overall sedimentary setting of a semi-restricted platform [18]. The Ordovician marine lithostratigraphic succession in this area, arranged in ascending order, comprises the Penglaiba Formation, Yingshan Formation, and Yijianfang Formation. Their lithological characteristics are as follows: ① The Penglaiba Formation is primarily composed of argillaceous micritic dolomite with minor sandy dolomite. ② The upper member of the Yingshan Formation is mainly interbedded with sandy limestone and micritic limestone, while the lower member is dominated by the interbedding of sandy limestone and dolomitic micritic limestone. ③ The Yijianfang Formation is mainly sandy limestone, containing some micritic limestone (Figure 1C).

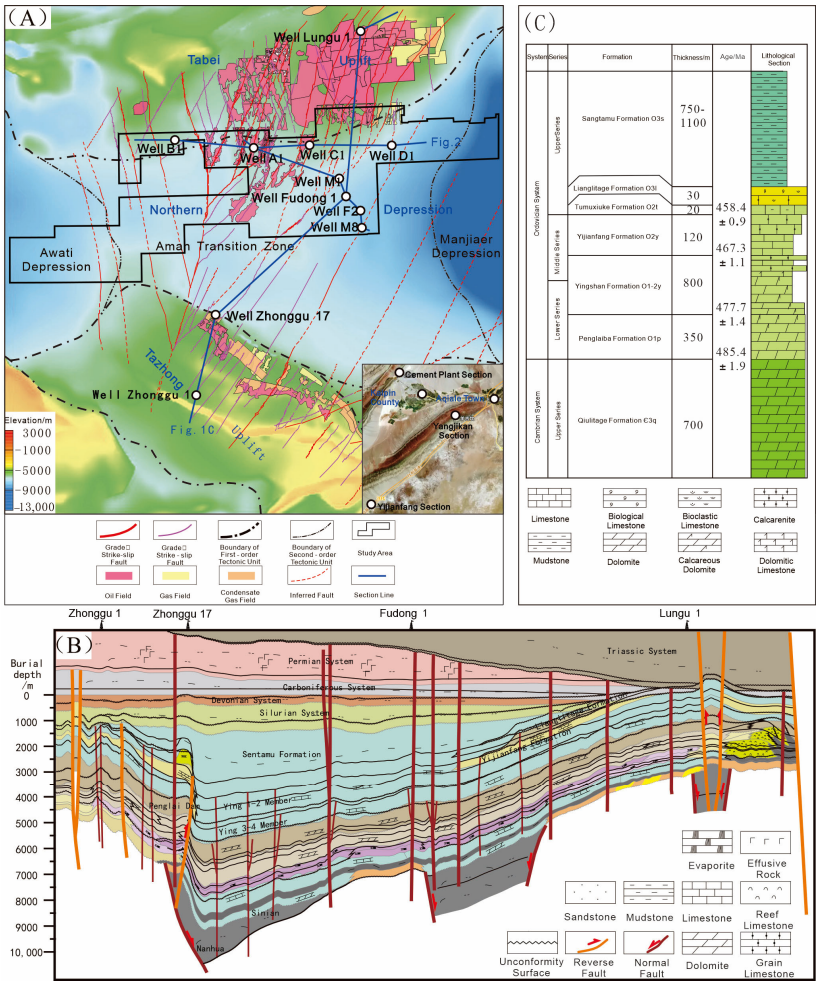


Figure 1. The structural map of the Awati–Manjiaer Depression transitional zone (**A**), the comprehensive histogram (**B**) and the large section map of the Carboniferous flattening structure (**C**).

3. Materials and Methods

This study made full use of various types of currently available data, encompassing conventional logging data, carbon isotope data, elemental logging data, field outcrop data, and field-measured magnetic susceptibility (MS) data from the Fuman Area. Specifically, the field outcrop data were acquired from the Penglaiba Formation of the Cement Plant Section, the Yingshan Formation of the Yangjikan Section, and the Yijianfang Formation of the Yijianfang Section within the Kalpin–Bachu area. For the collection of MS data, an MS-30 magnetometer was adopted, with samples collected at 5 cm intervals from the Penglaiba Formation of the Kalpin Cement Plant Section. Regarding the gamm-aray (GR) data of the Yangjikan Section, an XHG-2000M portable digital multi-channel gamma spectrometer (Sichuan XinxianDa Measurement and Control Technology Co., Ltd., Chengdu, China) was utilized to conduct point scanning at 20 cm intervals on the fresh surface of the section, thereby obtaining a continuous sequence of natural gamma data.

The stratigraphic framework was established through sequence stratigraphic principles for third-order sequence subdivision, with the research theory primarily based on this methodological approach [19]. The methods used for identifying classic sequence boundaries are as follows:

(1) Logging curves can identify vertical sedimentary evolution characteristics, among which the GR curve is commonly used to analyze the presence of unconformities. When the sequence boundary is a sedimentary discontinuity, the clay content increases, and the content of radioactive elements increases accordingly. This can cause the GR value at the boundary to increase, showing a serrated peak, and is often accompanied by characteristics such as decreased resistivity [20]. Revised Text: The Th/K ratio serves as a key indicator for characterizing clay mineral assemblages and inferring depositional environments, while also functioning as a proxy for relative fluctuations in the sedimentary base level [21]. A high Th/K ratio mainly indicates a weathering and exposure environment, while a low Th/K ratio represents a subaqueous sedimentary environment. The Th/U ratio can effectively indicate changes in redox environments.

(2) Stable carbon isotopes serve as key indicators of global relative sea-level changes. Elevated sea levels promote the preservation of sedimentary organic matter, corresponding to positive $\delta^{13}C$ excursions in inorganic carbonates, while lower sea levels drive negative isotopic shifts [22].

(3) Near unconformities, there are often characteristics of inert element enrichment and mobile element loss. Due to the influence of late diagenesis, the elemental characteristics may not reflect the original sedimentary conditions, but they can still be used as one of the auxiliary indicators for judging sequence boundaries. In field outcrops, sequence boundaries are relatively easy to identify. Stratigraphic unconformities are often accompanied by exposure and erosion, leading to identification marks such as dissolved pores, collapsed breccias, and weathering crusts at the boundary. Changes in some lithological and lithofacies assemblages can also serve as marks and bases for sequence division.

Climate proxies in sedimentary rocks preserve a variety of information, including "signals" generated by orbital cycle effects, water depth-related noise (e.g., storms, tides, bioturbation), and factors not controlled by orbits (e.g., dating errors, differential compaction, unstable sedimentation, and diagenesis). Additionally, depth-dependent noise variations at a fixed location may correlate with sea-level changes: lower noise levels correspond to higher relative sea levels, and vice versa. The DYNOT model, a sedimentary noise framework designed to assess two key components (total energy spectrum derived from orbitally tuned data and energy spectrum corresponding to non-astronomically driven signals), was developed [23]. The theoretical basis of the DYNOT model lies in its ability to separate orbital signals (eccentricity, obliquity, precession) from non-orbital "noise"

influenced by sea-level changes, making it particularly applicable for reconstructing paleo–sea-level fluctuations in carbonate systems like the Ordovician of the Tarim Basin. To date, this model has been widely adopted and applied in a multitude of relevant research studies. Empirical evidence from these applications consistently confirms that the sedimentary noise model serves as an effective and reliable method for the reconstruction and numerical simulation of paleo–sea-level changes [24–29]. Therefore, when effective methods for dividing high-frequency sequences are lacking, this model can be used to restore paleo-water depth as an identification mark.

Based on the Acycle 2.7 software under the MATLAB platform [30], this study employed two paleoclimate proxies—gamma-ray (GR) and magnetic susceptibility (MS) log data—to perform cyclostratigraphic investigations and establish a high-resolution sequence stratigraphic framework for fourth-order sequence subdivision. The data preprocessing workflow included the following: (1) data standardization using Z-score normalization to minimize scale effects; (2) linear interpolation to ensure equidistant sampling and address minor gaps; (3) detrending via first-order polynomial fitting to remove long-term background trends unrelated to orbital cycles; and (4) spectral normalization to enhance the signal-to-noise ratio.

The main steps are as follows:

(1) Preprocessing (including standardizing the data and removing long-term background trends);

(2) Performing spectral analysis on the GR and MS data sequences using the multitaper method (MTM), mainly analyzing peak frequencies with a confidence level of over 95% [31];

(3) Conducting Gaussian band-pass filtering on the peaks corresponding to the inferred 405 kyr long eccentricity cycle;

(4) Establishing an age model using the filtered 405 kyr long eccentricity cycle and performing tuning;

(5) Sea-level change trends were evaluated using the sedimentary noise model on orbitally tuned time-domain data. The DYNOT framework was applied with key parameters: total variance cutoff frequencies (fmin, fmax) set to 0.001 kyr^{-1} and 1 kyr^{-1}, respectively; a 405 kyr sliding window (aligned with the long eccentricity cycle); and 5000 Monte Carlo simulations for confidence interval assessment [8]. Here, P(e), P(o), and P(p) denote the energy values of eccentricity, obliquity, and precession, respectively.

Astronomical tuning of data sequences to the time domain mitigated variable sedimentation rate effects. Next, the ratio of non-orbital to total variance in the DYNOT model-derived power spectrum was used as a metric for quantifying noise in climate and sea-level proxies. Finally, the DYNOT value—defined as the ratio of non-orbital signal variance to total variance—was computed within a sliding time window.

$$R = 1 - \frac{P_{(e)} + P_{(o)} + P_{(P)}}{\sum_{i=f_{min}}^{f_{max}} P_{(i)}}$$

A 405 kyr sliding window and 5000 Monte Carlo simulations (for confidence interval evaluation) were used, with other parameters set to the defaults recommended [32].

4. Division of Third-Order Sequence Stratigraphy

Based on classic sequence division methods (logging curves, carbon isotopes, and field outcrop observations), this study identified five sequence boundaries that define third-order sequences across Well A1, the Kalpin Cement Plant Section, the Yangjikan Section, and the Yijianfang Section. These boundaries correspond to type-1 unconformities (subaerial exposure) and type-2 conformities (correlative surfaces), reflecting base-level changes

of ~0.5–3 Ma duration, consistent with third-order sequence stratigraphic frameworks. These boundaries are specified as follows: the unconformity surface at the top of the Cambrian System (T0); the unconformity surface at the top of the Lower Ordovician Penglaiba Formation (T1); the internal unconformity surface within the Middle-Lower Ordovician Yingshan Formation (T2); the unconformity surface at the top of the Middle-Lower Ordovician Yingshan Formation (T3); and the unconformity surface at the top of the Yijianfang Formation (located between the Upper Ordovician and Middle-Lower Ordovician) (T4).

4.1. Characteristics of Third-Order Sequence Boundaries in Well A1 of the Fuman Area

T4 boundary (top of the Yijianfang Formation): There is an abrupt lithological change above and below the boundary (Figure 2). The upper part is in contact with the mudstone of the Tumuxiuke Formation, while the lower part consists of argillaceous limestone. Logging curves show an abnormal sharp increase in GR, reflecting the characteristic of increased radioactivity above this boundary. The values of RS and RD curves are smaller above the boundary and significantly higher below it, indicating a change in the content of sandy clasts in the strata. The carbon isotope values in this stratum range from −0.46‰ to 1.20‰, with an average of 0‰, showing an upward trend from bottom to top with an increase of approximately 1.74‰. A negative shift of 0.5‰ in carbon isotopes occurs at the boundary, reflecting a sea-level fall during the sedimentary period.

T3 boundary (top of the Yingshan Formation): Strata below the boundary are dominated by sandy limestone, while strata above show a transition to sandy micritic limestone of the Yijianfang Formation (Figure 2). This contact exhibits a notable decrease in clay content, coinciding with a regional sea-level fall recorded by a −0.52‰ negative carbon isotope shift at the sequence boundary. The Yingshan Formation's first and second members display upward-increasing $\delta^{13}C$ values (−3.85‰ to −0.52‰, average −1.16‰), interpreted as transgressive deposition during relative sea-level rise preceding the boundary.

T2 boundary (internal to the Yingshan Formation): Above the boundary, strata comprise sandy micritic limestone, whereas underlying strata are sandy limestone enriched in dolomite. Geochemical proxies reveal abrupt changes: terrestrial elements (Fe, Ti) peak at the boundary, contrasting with depleted mobile elements (K), suggesting enhanced continental weathering and reduced marine influence during sequence boundary formation. This aligns with mixed-water dissolution patterns observed in analogous Cambrian strata.

T1 boundary (top of the Penglaiba Formation): The boundary separates argillaceous micritic dolomite (below) from dolomitic sandy limestone (above), marked by lithological abruptness and regional unconformity. This surface corresponds to a regional sea-level lowstand, with associated karstification and dolomitization processes documented in adjacent sections. In terms of logging response at the boundary, the natural gamma curve shows a sharp peak of 144.9 API, increasing from low to high above and below the boundary. The resistivity curve changes from the low-resistivity characteristic of dolomite to the high-resistivity characteristic above the boundary. The corresponding Th/K ratio also shows a sharp peak of 2.732, which is less than 7 and does not meet the standard of a weathering exposure surface. However, the Th/K ratio here varies frequently between 0.007 and 2.732 with a large amplitude, and the corresponding U value reaches the maximum of 15.1, indicating a sea-level fall in this area. The carbon isotope values in this stratum range from −2.28‰ to −1.70‰, with an average of −1.97‰. The carbon isotope value at the boundary is −1.92‰, showing a negative shift of approximately 1.10‰.

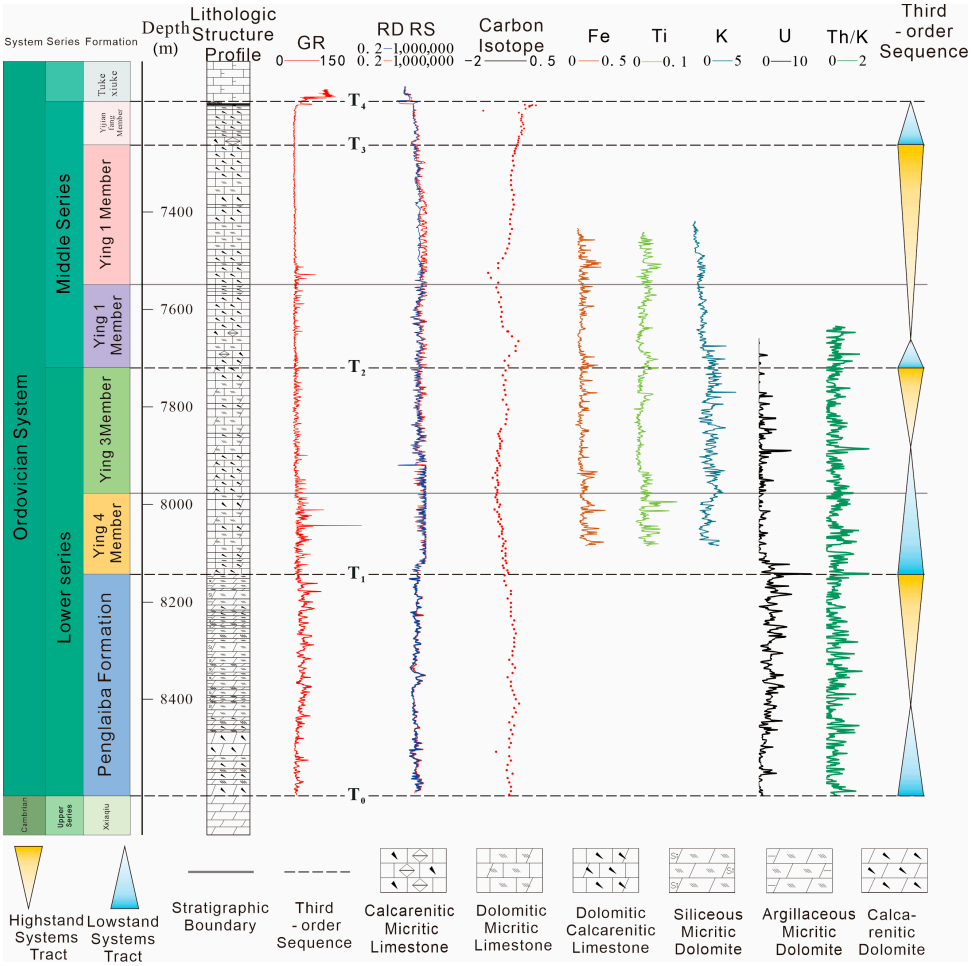


Figure 2. The third-order sequence interface characteristics of well A1.

Since there are currently no wells in the Fuman Area that penetrate the T0 boundary (at the bottom of the Penglaiba Formation), the logging response characteristics at the bottom of the Penglaiba Formation will not be discussed.

This study delineated maximum flooding surfaces (MFS) within third-order sequences through integrated analyses of lithology, carbon isotopes, and wireline logs. Notably, the O-SQ4 sequence in the Yijianfang Formation, attributed to prolonged subaerial exposure and significant denudation, preserves only a lowstand systems tract (LST), with no MFS recognized. At the MFS levels of the Yingshan Formation's first and second members, micritic limestone dominates the lithology, accompanied by a positive $\delta^{13}C$ excursion that culminates in a pronounced peak within these stratigraphic intervals. For the MFS of the O-SQ2 sequence in the third and fourth members of the Yingshan Formation, the lithology is dolomitic micritic limestone; the carbon isotope shows no obvious response within these members, but Th/K and U values in logging curves reach peaks here. The Penglaiba Formation has a short denudation duration; its MFS is characterized by argillaceous micritic dolomite, and the carbon isotope curve shows a positive shift with the largest amplitude within this formation, while other characteristic responses are not significant.

4.2. Characteristics of Third-Order Sequence Boundaries in the Kalpin–Bachu Area

Based on the characteristics of lithologic–lithofacies transition surfaces, paleoweathering crusts, and stratigraphic contact relationships observed in outcrop sections, this study identified four major third-order sequence boundaries within the Yijianfang Formation, Yingshan Formation, and Penglai Dam Formation in the Kalpin–Bachu area (Figure 3). With

respect to the T4 boundary, in the Yijianfang Section, the strata beneath this boundary consist of light gray, thin-bedded bioclastic micrite limestone, showing a conformable contact with the thin-bedded red argillaceous limestone at the base of the Tumuxiuke Formation (Figure 3A). Regarding the T3 boundary, the upper part of the Yangjikan Section belongs to the Dawangou Formation. This sequence boundary exhibits a parallel unconformable contact between the overlying and underlying strata. Specifically, the underlying strata consist of oolitic limestone from the Yingshan Formation, which indicates a high-energy bank depositional environment. In contrast, the overlying strata of the boundary are composed of nodular micrite limestone, bioclastic-bearing micrite limestone, and siliceous bands of the Dawangou Formation. In the Yijianfang Section, the lower part of the T3 boundary is characterized by massive gray–white marble, which forms an angular unconformable contact with the gray medium-bedded micrite limestone at the base of the Yijianfang Formation (Figure 3B). With regard to the T2 boundary, in the Yangjikan Section, the underlying strata of this boundary are composed of medium-thin-bedded micrite limestone interbedded with oolitic limestone of variable thickness. This unit forms a parallel unconformable contact with the overlying strata of the boundary—thin-bedded argillaceous limestone interbedded with thick-bedded oolitic micrite limestone of variable thickness (Figure 3C). For the T1 boundary, in the Cement Plant Section, light gray thin-bedded oolitic limestone establishes an angular unconformable contact with the overlying thick-bedded gray micrite limestone of the Yingshan Formation. Within this interval, the dolomite content decreases gradually until it is completely absent, and the lithology transitions from dolomite and dolomitic limestone to granular limestone. This lithologic variation indicates a significant shift in the depositional environment (Figure 3D). As for the T0 boundary, in the Cement Plant Section, it is manifested as a lithologic transition surface. The overlying strata of this boundary comprise a set of massive gray–white limestones, which form a conformable contact with the underlying gray dolomite of the Lower Qiulitage Formation of the Cambrian System (Figure 3E).

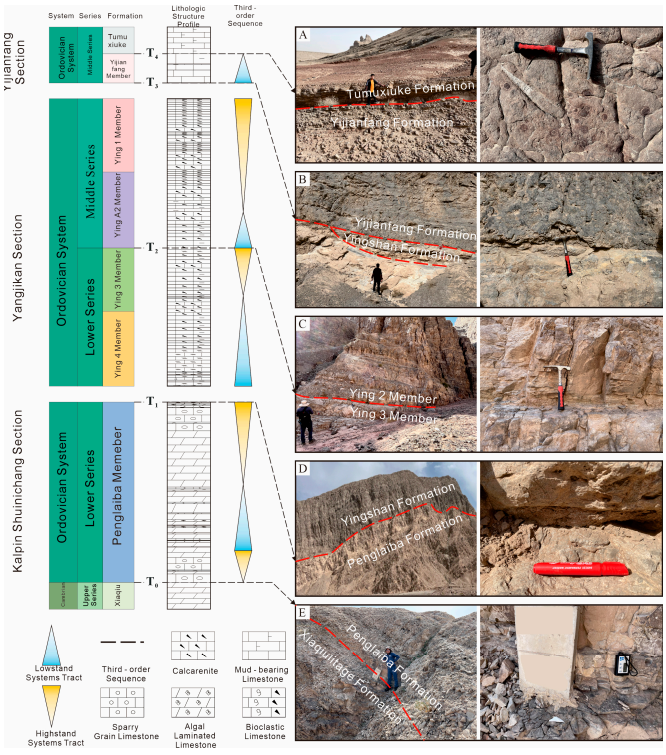


Figure 3. Characteristics of field third-order sequence interface.

5. Fourth-Order Sequence Stratigraphic Division

Fourth-order sequences are formed within third-order sequences under the control of secondary sea-level fluctuations caused by eccentricity variations, and they are isochronous in small areas [33]. Their boundary characteristics are short-term weathering exposure surfaces or regressive–transgressive cycle transition surfaces. There are a large number of exposure unconformity surfaces formed by multiple short-term sea-level drops in the Tarim Basin, which are controlled by sequences below the third order [34]. Therefore, based on the previously established framework of third-order sequence division, this study processes various sets of data by separating them at sequence boundaries to divide fourth-order sequences, providing an exploration basis for reservoirs formed by local exposure dissolution. Due to the lack of effective identification markers, a sedimentary noise model is introduced to reconstruct sea levels for identification. However, regarding the study of eccentricity variations, there is no relatively reliable astronomical orbital cycle scheme for the Ordovician System. Given that the 405 kyr long eccentricity cycle represents the most stable astronomical orbital parameter, prior studies have routinely employed it as the foundational geological time unit for calibrating the age of relatively ancient strata [35]. Meanwhile, due to the large time span of 400,000 years, it is not easily disturbed by small sedimentary gaps or other noises. Therefore, this study can achieve astronomical calibration by using the stable 405 kyr long eccentricity cycle.

5.1. Cyclostratigraphic Analysis

Based on the identification of third-order sequence boundaries, and for the purpose of mitigating the influence of sedimentary gaps, this study divides the gamma-ray (GR) data of the Yijianfang Formation–Penglaiba Formation interval in Well A1 into six relatively continuously deposited data segments. These segments include the Yijianfang Formation, the Ying 1–2 Members, the Ying 3–4 Members, the Penglaiba Formation, the Magnetic Susceptibility (MS) data of the Penglaiba Formation in the Kalpin Cement Plant Section, and the GR data of the Yingshan Formation in the Yangjikan Section. Subsequent to data preprocessing and the removal of long-term trends, spectral analysis was conducted. The theoretical orbital cycles selected for this analysis were calculated in accordance with the Milankovitch calculator model proposed by Waltham D. (2015), and the corresponding results are presented in Table 1 [36].

Table 1. Theoretical astronomical orbital period of Middle-Lower Ordovician.

Stratum	Stage	Median Age Ma	Long-eccentricityKyr	Short-eccentricityKyr		ObliquityKyr		PrecessionKyr	
Yijianfang Member	Darriwilian Stage	462.85	405	125	95	33.1003 ± 3.8692	20.7465 ± 1.5111	19.7328 ± 1.3734	17.0164 ± 1.0625
Ying1-2 Members	Dapingian Stage	468.65	405	125	95	33.0202 ± 3.8979	20.7136 ± 1.5254	19.7029 ± 1.3865	16.994 ± 1.0726
Ying3-4 Members	Floian Stage	473.85	405	125	95	32.9487 ± 3.9234	20.6841 ± 1.5381	19.6762 ± 1.3981	16.9739 ± 1.0816
Penglaiba Members	Tremadocian Stage	481.55	405	125	95	32.8433 ± 3.9606	20.6407 ± 1.5568	19.6367 ± 1.4153	16.9433 ± 1.0948

The multi-window spectral analysis method was used to conduct depth-domain spectral analysis on the detrended GR data sequence (Figure 6A–D). Among the results are the following:

For the Yijianfang Formation in Well A1, the spectral analysis shows prominent peaks corresponding to cycle thicknesses of 23.8 m, 5.4 m, 2.5 m, and 1.4 m, all with confidence

levels greater than 90% and some exceeding 99% (Figure 4A(a)). Based on the theoretical orbital cycle ratio of 405:100:33:19, these peaks are considered to correspond to the 405 kyr long eccentricity cycle, −100 kyr short eccentricity cycle, 33 kyr obliquity cycle, and −19 kyr precession cycle, respectively. For the Ying 1–2 Members in Well A1, prominent peaks are observed at cycle thicknesses of 57.2 m, 11.9 m, 3.3 m, 1.9 m, 1.6 m, and 1.4 m, with most confidence levels above 99% (Figure 4B(b)). Similarly, peaks at 57.2 m, 11.9 m, 3.3 m, and 1.9–1.4 m correspond to the 405 kyr long eccentricity cycle, 100 kyr short eccentricity cycle, 33 kyr obliquity cycle, and 19kyr precession cycle, respectively. For the Ying 3–4 Members in Well A1, prominent peaks appear at 31.5 m, 6.7 m, 2.9 m, 2 m, 1.4 m, 1.2 m, and 1.1 m, all with confidence levels exceeding 99% (Figure 4C(c)). The 31.5 m peak corresponds to the 405 kyr long eccentricity cycle, the 6.7 m peak to the −100 kyr short eccentricity cycle, the 2.9 m and 2 m peaks to the 33 kyr obliquity cycle, and the 1.4 m, 1.2 m, and 1.1 m peaks to the −19 kyr precession cycle. For the Penglaiba Formation in Well A1, prominent peaks are found at 21.4 m, 5.2 m, 1.8 m, and 1.1 m, all with confidence levels greater than 95% (Figure 4D(d)). These are respectively assigned to the 405 kyr long eccentricity cycle, −100 kyr short eccentricity cycle, 33 kyr obliquity cycle, and −19 kyr precession cycle. For the Penglaiba Formation in the Kalpin Cement Plant Section, prominent peaks occur at 18.8 m, 4.7 m, 3.1 m, 2 m, 1.6 m, and 1.2 m, all with confidence levels above 99% (Figure 4E(e)). The 18.8 m, 4.7–3.1 m, 2–1.6 m, and 1.2 m cycles correlate sequentially with 405 kyr eccentricity, 100 kyr eccentricity, 33 kyr obliquity, and 19 kyr precession cycles. For the Ying 1–2 Members of the Yingshan Formation in the Yangjikan Section, prominent peaks are observed at 12.4 m, 3.6 m, 0.98 m, and 0.55 m, with most confidence levels exceeding 99% (Figure 4F(f)). The 12.4 m cycle thickness corresponds to the 405 kyr long eccentricity cycle, the 3.6 m to the –100 kyr short eccentricity cycle, the 0.98 m to the 33 kyr obliquity cycle, and the 0.55 m to the −19 kyr precession cycle. For the Ying 3–4 Members of the Yingshan Formation in the Yangjikan Section, prominent peaks appear at 15.6 m, 3.9 m, 1.5 m, and 0.75 m, all with confidence levels greater than 99% (Figure 4G(g)). The cycle thicknesses of 15.6 m, 3.9 m, 1.5–1.6 m, and 0.75 m mirror the 405 kyr eccentricity, 100 kyr short eccentricity, 33 kyr obliquity, and 19 kyr precession cycles in sequence.

Multitaper spectral analysis (MTM) was performed with a time-bandwidth product of 2 and 3 orthogonal tapers, utilizing adaptive window sizing for detrended data. A Gaussian band-pass filter (central frequency: 0.00247 kyr^{-1}, bandwidth: ±0.0005 kyr^{-1}) isolated the 405 kyr eccentricity cycle from the detrended sequences. Filter parameters were optimized to isolate orbital signals (eccentricity, obliquity, precession) while minimizing noise. Results show prominent peaks aligned with theoretical Milankovitch cycles for each formation (e.g., 23.8 m, 5.4 m cycles in the Yijianfang Formation).

The frequency band corresponding to the 405 kyr long eccentricity cycle was extracted from the GR data sequence for filtering processing (Figure 4A–D). The results are as follows:

Filtering analysis of the Yijianfang Formation (Well A1) yielded four cycles of the 405-kyr eccentricity, corresponding to a sedimentary duration of 1.6 Ma. For the Ying 1–2 Members (Well A1), eight cycles of the 405 kyr eccentricity were identified, with a duration of 3.2 Ma. The Ying 3–4 Members (Well A1) exhibited 12 cycles of the 405 kyr eccentricity, corresponding to 4.9 Ma of sedimentation. The Penglaiba Formation (Well A1) showed 12 cycles of the 405 kyr eccentricity, with a sedimentary duration of 4.9 Ma. Analysis of the Penglaiba Formation (Kalpin Cement Plant Section) revealed 15 cycles of the 405 kyr eccentricity, corresponding to 6.1 Ma. For the Ying 1–2 Members of the Yingshan Formation (Yangjikan Section), seven cycles of the 405 kyr eccentricity were determined, with a duration of 2.8 Ma. The Ying 3–4 Members of the Yingshan Formation (Yangjikan Section) had 10 cycles of the 405 kyr eccentricity, corresponding to 4.1 Ma of sedimentation.

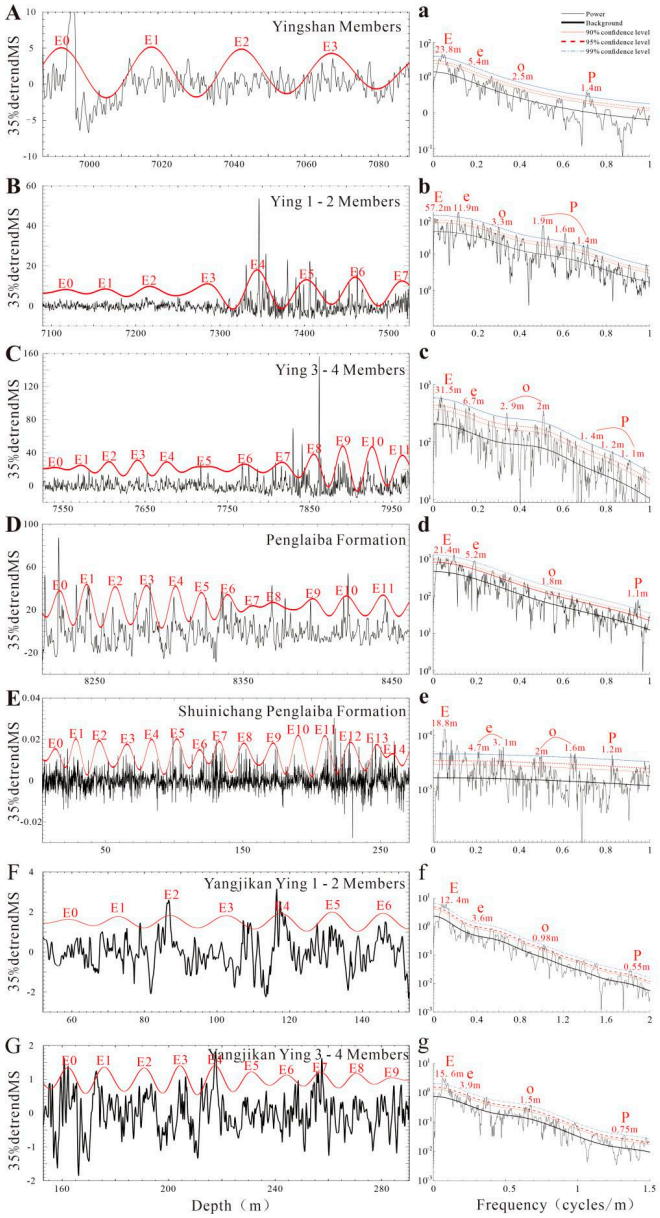


Figure 4. Spectrum analysis and depth domain filtering.

While the cyclostratigraphic analysis demonstrates robust orbital signals (e.g., 405 kyr eccentricity cycles) with high statistical confidence (>90–99%), uncertainties in deep-time orbital parameters require consideration. These uncertainties primarily stem from (1) potential deviations in astronomical constants (e.g., precession and obliquity periods) during the Ordovician period due to chaotic Solar System dynamics; (2) errors in geological age models affecting orbital tuning precision; and (3) noise from sedimentary processes (e.g., hiatuses, diagenesis). The DYNOT model partially mitigates these by decoupling orbital signals from local depositional noise, yet absolute chronological accuracy may be influenced by the assumed stability of Phanerozoic orbital parameters. Future studies integrating Paleozoic-specific dynamical astronomical models could further refine these chronostratigraphic constraints.

5.2. Sea-Level Simulation Based on the Sedimentary Noise Model

Based on the stable 405 kyr long eccentricity cycle, the relative sea-level change trends of each geological segment were obtained through comprehensive analytical calculations

using the DYNOT model algorithm [36]. The specific variation characteristics of these trends are presented in Figure 5, and the key analytical results are summarized as follows:

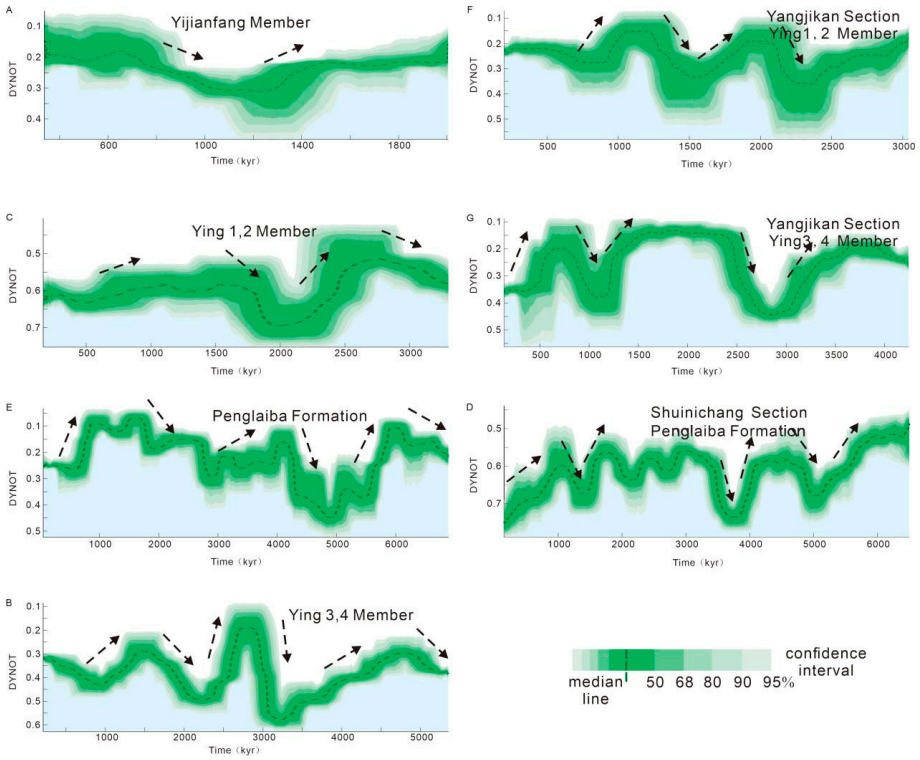


Figure 5. Sedimentary noise model to reconstruct sea level.

The Yijianfang Formation in Well A1 exhibited a sea-level change trend of first falling and then rising within 1.6 Ma.

The Ying 1–2 Members of the Yingshan Formation in both Well A1 and the Yangjikan Section lasted for approximately 3 Ma, while the Ying 3–4 Members lasted for about 4.5 Ma. Cyclostratigraphic analysis of the GR data from these two locations revealed that the sea levels of the Yingshan Formation in the field outcrops and the Fuman Area showed similar characteristics of fluctuation frequency within comparable time scales.

The Penglaiba Formation in both Well A1 and the Kalpin Cement Plant Section had a duration of around 6 Ma. Sea-level simulation using the sedimentary noise model based on the magnetic susceptibility data from the Kalpin Cement Plant Section showed that the Penglaiba Formation in the field outcrops and the Fuman Area experienced three consistent cycles of sea-level rise and fall within similar time scales.

Sea-level changes were simulated using the DYNOT model with key parameters: cutoff frequencies for total variance (fmin = 0.001 kyr^{-1}, fmax = 1 kyr^{-1}), a sliding window size of 405 kyr (aligning with the long eccentricity cycle), and 5000 Monte Carlo simulations to evaluate confidence intervals. The model separates orbital signals from non-orbital noise, with the ratio of non-orbital variance to total variance (DYNOT value) serving as a proxy for paleo–sea-level fluctuations. Results are consistent with field-observed sequence boundaries (e.g., dissolution pores in the Yijianfang Formation).

Depth–time calibration was achieved via orbital forcing analysis of the 405 kyr eccentricity cycle, translating drilling depths into stratigraphic ages (e.g., 1.6 Ma for the Yijianfang Formation at Well A1). The analysis utilized gamma-ray (GR) data from Well A1 and magnetic susceptibility (MS) data from the Kalpin Cement Plant Section. The methodological workflow included data preprocessing (detrending, normalization), spectral analysis via the multitaper method (MTM), and Gaussian band-pass filtering to isolate orbital cy-

cles, followed by DYNOT-based reconstruction of sea-level trends from the sedimentary noise signals.

5.3. Characteristics of Fourth-Order Sequence Boundaries in Field Outcrops and Their Corresponding Relationship with the Fuman Area

Revealed through detailed investigation of lithostratigraphic discontinuities and regional unconformities (Figure 6), the Ying 1–2 Members of the Yingshan Formation in the Yangjikan Section can be divided into two fourth-order sequences, and the Ying 3–4 Members into three fourth-order sequences; the Ying 1–2 Members of the Yingshan Formation in the Kalpin Cement Plant Section can be divided into two fourth-order sequences, the Ying 3–4 Members into three fourth-order sequences, and the Penglaiba Formation into three fourth-order sequences.

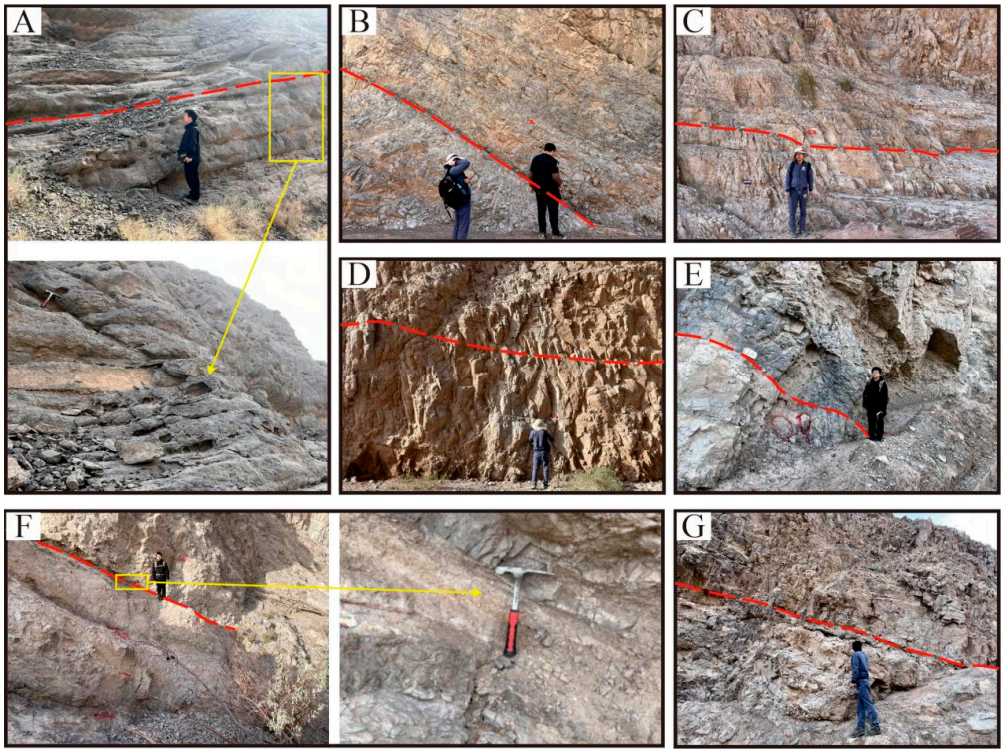


Figure 6. Field characteristics of fourth-order sequence.

Specifically, above the T41 boundary of the Yijianfang Formation in the Yijianfang Section is dark gray thin-bedded bioclastic limestone, and below the boundary is medium-thick-bedded dark gray bioclastic limestone with a large number of dissolution pores (with a diameter of approximately 5~20 cm) (Figure 6A). The T31 boundary in the Ying 1–2 Members (Yangjikan Section) constitutes a conformable lithostratigraphic contact between upper dark gray medium-thin-bedded micritic limestone and lower gray–dark gray thin-bedded micritic limestone, marked by an upward-lightening lithologic gradation (Figure 6B); above the T22 boundary of the Ying 3–4 Members is gray thin-bedded micritic limestone with horizontal bedding, and the lower part is interbedded with gray medium-bedded calcarenite, with dissolution pores observed (Figure 6C). Above the T21 boundary is interbedded gray medium-thin-bedded micritic limestone and thin-bedded argillaceous limestone, and below the boundary is gray medium-thick-bedded calcarenitic micritic limestone, with dissolution pores present (Figure 6D). In the Kalpin Cement Plant Section, the T31 boundary of the Ying 1–2 Members of the Yingshan Formation is a lithological transition surface, transitioning from dark gray medium-bedded sparry grain limestone to off-white thin-bedded bioclastic limestone; the T22 boundary of the Ying 3–4 Members transitions from interbedded gray

thin-bedded algal laminated limestone and grain limestone to gray medium-thick-bedded bioclastic limestone. The T21 boundary exhibits thin interbedding of gray bioclastic limestone and algal laminated limestone, grading into gray medium-thick-bedded bioclastic limestone. In the outcrop of the Penglaiba Formation, the T11 boundary is a lithological transition surface with an abrupt color change from light gray to dark gray; the lithology is conformable contact between off-white massive dolomite and the overlying grayish-black medium-thin-bedded calcarenite (Figure 6E). The strata above and below the T12 boundary show obvious angular unconformity contact, with a paleoweathering crust about 30 cm thick and a significant increase in argillaceous content (Figure 6F); the overall lithology around the T13 boundary is off-white medium-thick-bedded argillaceous limestone, with multiple phases of weathering crusts (about 3–5 cm thick) developed near the boundary, indicating that the Penglaiba Formation underwent multiple frequent and short-term uplift and exposure during this period (Figure 6G).

A comparison between the fourth-order sequence boundaries identified based on field characteristics and the results of cyclostratigraphic analysis and sea-level simulation shows that the sea-level fluctuations reconstructed by the sedimentary noise model are consistent with the field identification markers, confirming that this model can be used for sea-level restoration of the Middle-Lower Ordovician carbonate rocks in the Tarim Basin. In the future, this method can be applied to the sequence stratigraphic division of ultra-deep carbonate rocks in the Fuman Area.

In addition, on the basis of the astronomical chronostratigraphic scales established respectively for the magnetic susceptibility data of the Penglaiba Formation in the Kalpin Cement Plant Section, the GR data of the Yingshan Formation in the Yangjikan Section, and the GR data of Well A1, a chronostratigraphic framework between the field outcrops and the Fuman Area was jointly established by combining sea-level change trends and carbon isotope data. The comparison shows (Figure 7) that the lower part of Well A1, the only well that has drilled through the Penglaiba Formation in the Fuman Area so far, is still missing one third-order sequence and one fourth-order sequence.

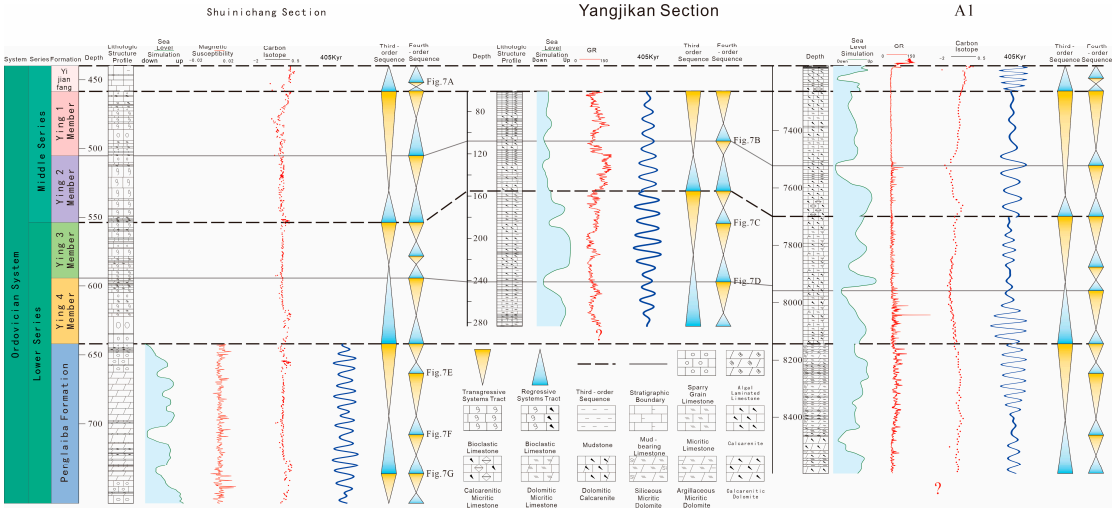


Figure 7. Sequence interface characteristics and correlation diagram of Keping Cement Plant profile–Yangjikan profile–A1 well.

6. Discussion

6.1. Sequence Division Scheme of the Fuman Area

Building upon previous research findings, this study comprehensively divided the third- and fourth-order sequences and proposed a sequence division scheme for the Ordovician carbonate rocks in the Fuman Area (Figure 8). The key third-order sequence

boundaries are basin-wide unconformity surfaces, with cross-regional and cross-facies belt comparability. Based on classic sequence division methods—including logging curves, carbon isotopes, and field outcrop observations—this study identified five sequence boundaries that define third-order sequences across Well A1, the Kalpin Cement Plant Section, the Yangjikan Section, and the Yijianfang Section. Specifically, the Yijianfang Formation is divided into one third-order sequence (O-SQ4), the Yingshan Formation into two third-order sequences (O-SQ2, O-SQ3), and the Penglaiba Formation into one third-order sequence (O-SQ1). This scheme is consistent with most sequence division frameworks proposed in prior studies. For example, the Yijianfang Formation's single sequence aligns with [37] identification of four comparable transgressive–regressive cycles in the Shuntuoguole uplift, while the Yingshan Formation's dual sequences match [38] subdivision of mixed-water dissolution intervals. The Penglaiba Formation's boundary, marked by abrupt lithological changes, mirrors [39] findings on karst-modified diagenetic surfaces in adjacent sections.

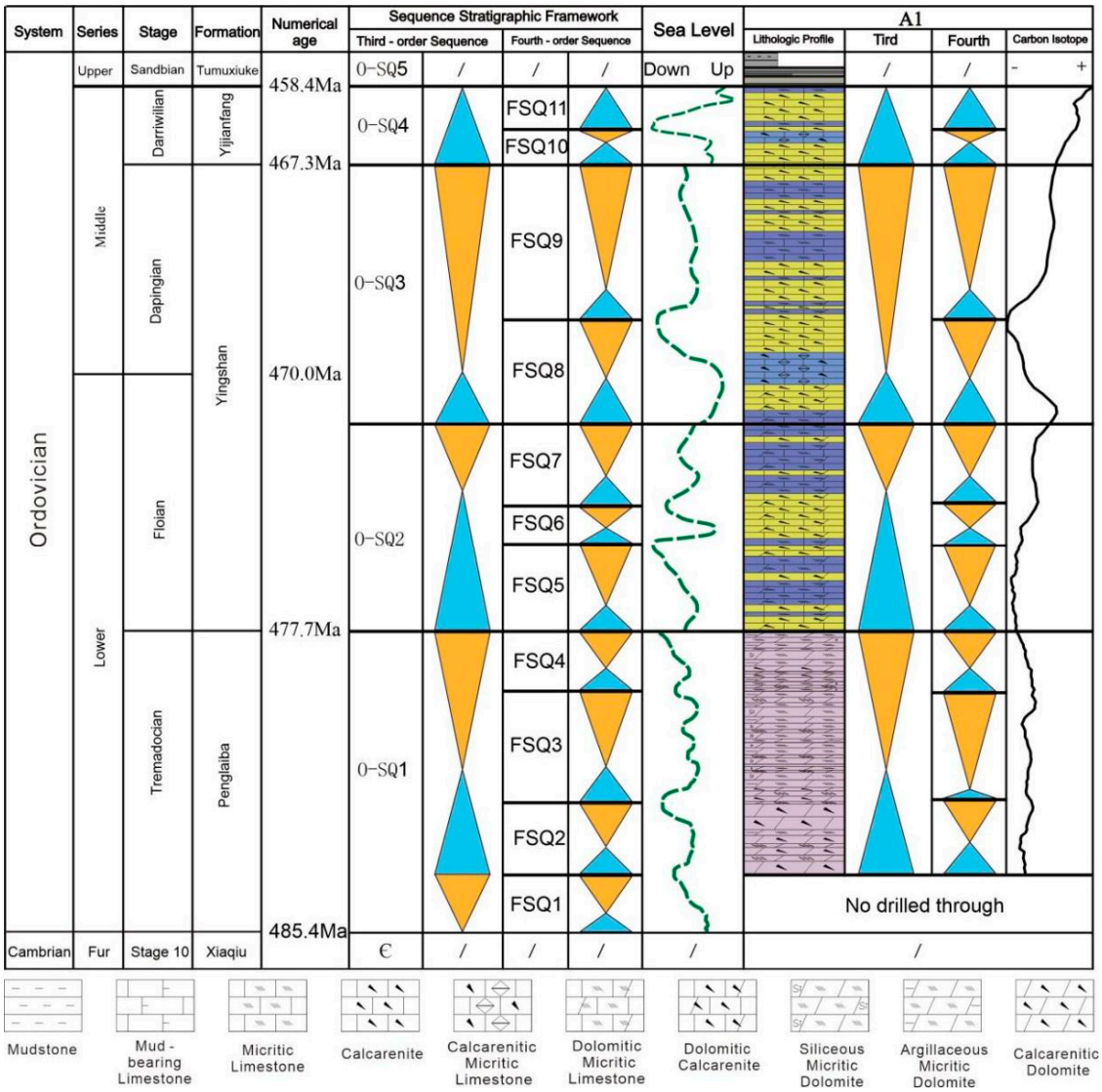


Figure 8. Sequence division scheme of well A1 based on DYNOT model.

Fourth-order sequences often show significant differences within the basin due to their diverse genetic types, small scale, and high frequency. This study attempts to carry out fourth-order sequence division by combining the classical sequence division method with sea-level reconstruction simulated by the sedimentary noise model. The field sequence

boundary characteristics of the Kalpin Cement Plant Section and the Yangjikan Section have a good corresponding relationship with the sea-level fluctuations simulated by the sedimentary noise model based on the measured GR and MS data sequences of the sections, which verifies the feasibility of the DYNOT model in identifying sea-level change trends in the Middle-Lower Ordovician of the Tarim Basin. Introducing the cyclostratigraphic method into the study of the Fuman Area revealed that the genetic types of fourth-order sequences in the study area are significantly controlled by sea level. Finally, the Yijianfang Formation is divided into two fourth-order sequences (FSQ10−11), the Ying 1–2 Members into two fourth-order sequences (FSQ8–9), the Ying 3–4 Members into three fourth-order sequences (FSQ5–7), and the Penglaiba Formation into four fourth-order sequences (FSQ1–4).

6.2. Coupling Relationship Between Sequence Stratigraphic Division and Reservoir Development

The composition of carbonate sequence system tracts determines the distribution characteristics of their sedimentary facies belts, and hydrocarbon accumulation is also controlled by system tracts to varying degrees. For example, favorable source rocks develop in highstand system tracts, while high-quality reservoirs can form in lowstand system tracts [40]. Applying the sedimentary noise modeling framework, this study reconstructed Middle-Lower Ordovician carbonate platform evolution in the Fuman Area through dynamic integration of astrochronological constraints and multi-proxy stratigraphic datasets. According to the reservoir classification standards of PetroChina Tarim Oilfield (Table 2), a comprehensive evaluation of logging porosity and permeability in Well M8-Well A1 was conducted for reservoir grading. It was found that high-quality reservoir intervals are predominantly developed within lowstand systems tracts (Figure 9), a pattern consistent with regional observations from the Tarim Basin and global analogs such as the Middle Ordovician carbonate platforms in the Yangtze region. This spatial correlation arises because lowstand system tracts are characterized by karstification processes triggered by subaerial exposure during sea-level fall. For instance, in the Fuman Area, lowstand intervals exhibit well-developed dissolution porosity (e.g., vuggy and intergranular porosity) formed through meteoric water circulation, as evidenced by $\delta^{13}C$ values (−3.85‰ to −0.52‰) indicating subaerial exposure events. These karst-modified strata enhance reservoir quality by creating interconnected pore networks, a mechanism similarly documented in high-frequency sequence frameworks of the Longwangmiao Formation. Therefore, restoring paleowater depth and mapping system tracts within relative sea-level cycles provides critical insights for predicting favorable reservoir distribution in similar tectonic settings.

Table 2. Reservoir classification standard.

Stratum	Sequence	Systems Tract	Response Characteristics of Maximum Flooding Surface		
			Lithologic Characteristics	Carbon Isotope Characteristics	Well Logging Curve Characteristics
Ying1–2 Members	O-SQ3	HST TST	Micritic Limestone	Positive Excursion	/
Ying1–2 Members	O-SQ2	HST TST	DolomiticMicritic Limestone	Not Significant Response	Th/KPeak2.36 UPeak15.91
Penglaiba Formation	O-SQ1	HST TST	Argillaceous Micritic Dolomite	Positive Excursion	Th/KPeak1.76 Other Curves with Not Significant Response

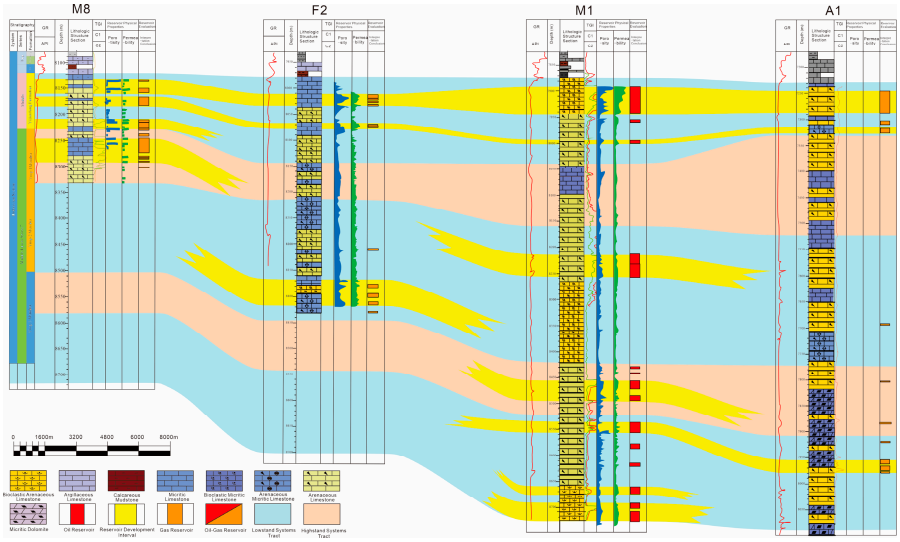


Figure 9. M8 well-F2, well-M1, well-A1 well reservoir comparison.

The sedimentary area of carbonate platforms is significantly controlled by third-order sea-level changes. With the periodic fall in sea level, sediments are exposed above the sea surface or located within the freshwater lens, undergoing selective and non-selective dissolution. This karstification is widely developed in the Tabei–Tazhong Area [41]. Based on cyclostratigraphic time series analysis, the residual stratigraphic age of the Yijianfang Formation in the Fuman Area is only 1.6 Ma, characterized by a long duration of meteoric freshwater leaching and large erosion thickness. Comprehensive rare earth and major-trace-element analyses were performed across multiple wells within the study area [42]. The findings revealed that the karst fracture-cave fillings in the Yijianfang Formation originated from meteoric freshwater sources and exhibited significant alterations due to terrigenous clastic influx. This indicates that the exposure below the third-order sequence boundaries has a significant impact on karst development and a positive effect on the physical property modification of reservoirs. In summary, the establishment of a detailed sequence stratigraphic framework in the Fuman Area can provide a basis for characterizing favorable sedimentary facies belts and exploring non-fault-controlled hydrocarbon reservoirs.

7. Conclusions

This study demonstrates the successful application of an integrated methodology combining conventional sequence stratigraphy with cyclostratigraphic analysis using the sedimentary noise model (DYNOT) to establish a high-resolution sequence stratigraphic framework for the Middle-Lower Ordovician carbonate rocks in the Fuman Area of the Tarim Basin. The consistency between sea-level changes simulated by the DYNOT model and sequence boundaries identified in field outcrops (e.g., Kalpin Cement Plant and Yangjikan sections) validates the reliability of cyclostratigraphy in reconstructing paleo–sea-level fluctuations. The Ordovician succession is divided into four third-order sequences (O-SQ1 to O-SQ4) and eleven fourth-order sequences (FSQ1 to FSQ11), providing a systematic stratigraphic framework for the Yijianfang, Yingshan, and Penglaiba Formations.

The refined sequence stratigraphic framework reveals a strong coupling between reservoir quality and system tracts, with high-quality reservoirs predominantly developed in lowstand system tracts influenced by exposure and karstification. This study not only confirms the preservation of astronomical orbital signals in Ordovician carbonates but also offers a practical, high-efficiency approach for sequence division using conventional logging data. The results provide a scientific basis for characterizing favorable sedimentary

facies and optimizing exploration strategies in non-fault zones, contributing significantly to ultra-deep oil and gas exploration in the Fuman Area.

Author Contributions: Conceptualization, H.X. and X.Z.; Methodology, P.S and C.S.; Validation, P.S. and T.L.; Formal Analysis, L.G. and T.L.; Investigation, C.S.; Resources, Z.X. and R.L.; Data Curation, L.G.; Writing—Original Draft Preparation, H.X.; Writing—Review and Editing, H.X., X.Z. and J.L.; Supervision, X.Z. and J.L.; Project Administration, R.L.; Funding Acquisition, Z.X. All authors have read and agreed to the published version of the manuscript.

Funding: This research was funded by the DeepEarth Probe and Mineral Resources Exploration—National Science and Technology Major Project [2025ZD1008901] and the National Natural Science Foundation of China [41772150]. The APC was funded by the same grant.

Data Availability Statement: The data presented in this study are available on request from the corresponding author due to restrictions. The seismic and well-logging data were provided by the Tarim Oilfield Company, PetroChina, under confidentiality agreements and are available from the authors with the permission of the third party. Field outcrop data are accessible through Southwest Petroleum University's institutional repository for academic purposes.

Acknowledgments: The authors extend their sincere appreciation to the Tarim Oilfield Company, PetroChina, for providing essential geological data and fieldwork support. We gratefully acknowledge the Sichuan Key Laboratory of Natural Gas Geology at Southwest Petroleum University for technical assistance and research facilities. Special thanks are due to the field investigation teams for their meticulous data collection efforts. We also thank the anonymous reviewers for their valuable suggestions and the editorial team of Geosciences for their professional handling of this manuscript.

Conflicts of Interest: Authors Xie Zhou, Sun Chong, Shi Pingzhou, and Liu Ruidong are employed by the Tarim Oilfield company. The remaining authors declare that the research was conducted in the absence of any commercial or financial relationships that could be construed as a potential conflict of interest.

References

1. Yang, H.J.; Chen, Y.Q.; Tian, J.; Du, J.H.; Zhu, Y.F.; Li, H.H.; An, H.T. Great discovery and its significance of exploration for Ordovician ultra-deep fault-controlled carbonate reservoirs of Well Manshen 1 in Tarim Basin. *China Pet. Explor.* **2020**, *25*, 13–23. (In Chinese)
2. Zhu, G.; Chen, F.; Wang, M.; Zhang, Z.; Ren, R.; Wu, L. Discovery of the lower Cambrian high-quality source rocks and deep oil and gas exploration potential in the Tarim Basin, China. *AAPG Bull.* **2018**, *102*, 2123–2151. [CrossRef]
3. Vail, P.R.; Colin, J.P.; Du Chene, R.J.; Kuchly, J.; Mediavilla, F.; Trifilieff, V. Sequence stratigraphy and its application to the chronostratigraphic correlation of the Paris basin Jurassic. *Bull. Soc. Geol. Fr.* **1987**, *3*, 1301. [CrossRef]
4. Abels, H.A.; Aziz, H.A.; Krijgsman, W.; Smeets, S.J.; Hilgen, F.J. Long-period eccentricity control on sedimentary sequences in the continental Madrid Basin (middle Miocene, Spain). *Earth Planet. Sci. Lett.* **2010**, *289*, 220–231. [CrossRef]
5. Boulila, S.; Galbrun, B.; Miller, K.G.; Pekar, S.F.; Browning, J.V.; Laskar, J.; Wright, J.D. On the origin of Cenozoic and Mesozoic "third-order" eustatic sequences. *Earth-Sci. Rev.* **2011**, *109*, 94–112. [CrossRef]
6. Mei, M.X. From vertical stacking pattern of cycles to discerning and division of sequences: The third advance in sequence stratigraphy. *J. Palaeogeogr.* **2011**, *13*, 37–54. (In Chinese)
7. Boulila, S.; Galbrun, B.; Huret, E.; Hinnov, L.A.; Rouget, I.; Gardin, S.; Bartolini, A. Astronomical calibration of the Toarcian Stage: Implications for sequence stratigraphy and duration of the early Toarcian OAE. *Earth Planet. Sci. Lett.* **2014**, *386*, 98–111. [CrossRef]
8. Li, M.; Hinnov, L.A.; Huang, C.; Ogg, J.G. Sedimentary noise and sea levels linked to land-ocean water exchange and obliquity forcing. *Nat. Commun.* **2018**, *9*, 1004. [CrossRef]
9. Liu, Q.; Shi, J.; Shen, Y. Volcanics-driven episodic events enhancing organic carbon accumulation in black shale during the Middle Eocene. *Geochim. Et Cosmochim. Acta* **2026**, *413*, 233–240. [CrossRef]
10. Jia, C.Z. Structural features and oil-gas accumulation rules in Tarim Basin. *Xinjiang Pet. Geol.* **1999**, *20*, 177–183. (In Chinese)
11. Qiming, L.; Guanghui, W.; Xiongqi, P.; Wenqin, P.A.N.; Chunshu, L.; Chenglin, W.; Bo, Z. Hydrocarbon accumulation conditions of Ordovician carbonate in Tarim Basin. *Acta Geol. Sin.* **2010**, *84*, 1180–1194. [CrossRef]

12. Zhang, S.C.; Hanson, A.D.; Moldowan, J.M.; Graham, S.A.; Liang, D.G.; Chang, E.; Fago, F. Paleozoic oil-source rock correlations in the Tarim Basin, NW China. *Org. Geochem.* **2000**, *31*, 273–286. [CrossRef]
13. Thompson, K.F.M. Light hydrocarbon in subsurface sediments. *Geochim. Cosmochim. Acta* **1979**, *43*, 657–672. [CrossRef]
14. Feng, Z.Z.; Bao, Z.D.; Wu, M.B.; Jin, Z.K.; Shi, X.Z.; Luo, A.R. Lithofacies palaeogeography of the Ordovician in Tarim Area. *J. Palaeogeogr.* **2007**, *9*, 447–460. (In Chinese)
15. Wu, G.H.; Li, Q.M.; Xiao, Z.Y.; Li, H.H.; Zhang, L.P.; Zhang, X.J. Evolution characteristics and oil-gas exploration of palaeouplifts in Tarim Basin. *Geotecton. Metallog.* **2009**, *33*, 124–130. (In Chinese)
16. Lin, C.; Yang, H.; Liu, J.; Rui, Z.; Cai, Z.; Li, S.; Yu, B. Sequence architecture and depositional evolution of the Ordovician carbonate platform margins in the Tarim Basin and its response to tectonism and sea-level change. *Basin Res.* **2012**, *24*, 559–582. [CrossRef]
17. Tian, J.; Yang, H.; Zhu, Y.; Deng, X.; Xie, Z.; Zhang, Y.; Huang, L. Geological conditions for hydrocarbon accumulation and key technologies for exploration and development in Fuman Oilfield, Tarim Basin. *Acta Pet. Sin.* **2021**, *42*, 971–985. (In Chinese)
18. Alexeiev, D.V.; Biske, Y.S.; Djenchuraeva, A.V.; Kröner, A.; Getman, O.F. Late Carboniferous (Kasimovian) closure of the South Tianshan Ocean: No Triassic subduction. *J. Asian Earth Sci.* **2019**, *173*, 54–60. [CrossRef]
19. Fisher, W.L.; McGowen, J.H. Depositional Systems in Wilcox Group of Texas and Their Relationship to Oil and Gas Occurrence: ABSTRACT. *AAPG Bull.* **1967**, *51*, 2163–2164. [CrossRef]
20. He, D.; Zhou, X.; Zhang, C.; Yang, X. Tectonic types and evolution of Ordovician proto-type basins in the Tarim region. *Chin. Sci. Bull.* **2007**, *52*, 164–177. [CrossRef]
21. Dai, D.J.; Tang, Z.S.; Chen, X.T. Geochemical characteristics of uranium and its logging response in oil and gas exploration. *Nat. Gas Ind.* **1995**, *15*, 21–24, 99–100. (In Chinese)
22. Gao, Z.Q.; Fan, T.L. Carbonate platform-margin architecture and its influence on Cambrian-Ordovician reef-shoal development, Tarim Basin, NW China. *Mar. Pet. Geol.* **2015**, *68*, 291–306. [CrossRef]
23. Li, M.; Kump, L.R.; Hinnov, L.A.; Mann, M.E. Tracking variable sedimentation rates and astronomical forcing in Phanerozoic paleoclimate proxy series with evolutionary correlation coefficients and hypothesis testing. *Earth Planet. Sci. Lett.* **2018**, *501*, 165–179. [CrossRef]
24. Muhs, D.R.; Simmons, K.R.; Schumann, R.R.; Halley, R.B. Sea-level history of the past two interglacial periods: New evidence from U-series dating of reef corals from south Florida. *Quat. Sci. Rev.* **2010**, *30*, 570–590. [CrossRef]
25. Solihuddin, T.; O'Leary, M.J.; Blakeway, D.; Parnum, I.; Kordi, M.; Collins, L.B. Holocene reef evolution in a macrotidal setting: Buccaneer Archipelago, Kimberley Bioregion, Northwest Australia. *Coral Reefs* **2016**, *35*, 783–794. [CrossRef]
26. Lu, Y.; Huang, C.; Jiang, S.; Zhang, J.; Lu, Y.; Liu, Y. Cyclic late Katian through Hirnantian glacioestasy and its control of the development of the organic-rich Wufeng and Longmaxi shales, South China. *Palaeogeogr. Palaeoclimatol. Palaeoecol.* **2019**, *526*, 96–109. [CrossRef]
27. Fang, Q.; Wu, H.; Wang, X.; Yang, T.; Li, H.; Zhang, S. An astronomically forced cooling event during the Middle Ordovician. *Glob. Planet. Change* **2019**, *173*, 96–108. [CrossRef]
28. Wang, M.; Li, M.; Kemp, D.B.; Boulila, S.; Ogg, J.G. Sedimentary noise modeling of lake-level change in the Late Triassic Newark Basin of North America. *Glob. Planet. Change* **2022**, *208*, 103706. [CrossRef]
29. Zhang, T.; Li, Y.; Fan, T.; Da Silva, A.C.; Shi, J.; Gao, Q.; Li, M. Orbitally-paced climate change in the early Cambrian and its implications for the history of the Solar System. *Earth Planet. Sci. Lett.* **2022**, *583*, 117420. [CrossRef]
30. Li, M.; Hinnov, L.; Kump, L. Acycle: Time-series analysis software for paleoclimate research and education. *Comput. Geosci.* **2019**, *127*, 12–22. [CrossRef]
31. Thomson, D.J. Spectrum estimation and harmonic analysis. *Proc. IEEE* **1982**, *70*, 1055–1096. [CrossRef]
32. Allen, J.R.; Wiggins, W.D. *Dolomite Reservoirs-Geochemical Techniques for Evaluating Origin and Distribution*; AAPG: Tulsa, OK, USA, 1993; p. 129.
33. Eriksson, P.G.; Catuneanu, O.; Nelson, D.R.; Popa, M. Controls on Precambrian sea level change and sedimentary cyclicity. *Sediment. Geol.* **2005**, *176*, 43–65. [CrossRef]
34. Ge, R.; Zhu, W.; Wilde, S.A.; He, J.; Cui, X.; Wang, X.; Bihai, Z. Neoproterozoic to Paleozoic long-lived accretionary orogeny in the northern Tarim Craton. *Tectonics* **2014**, *33*, 302–329. [CrossRef]
35. Loucks, R.G.; Sarg, J.F. Carbonate sequence stratigraphy: Recent developments and applications. *AAPG Mem.* **1993**, *57*, 1–515.
36. Waltham, D. Milankovitch Period Uncertainties and Their Impact on Cyclostratigraphy. *J. Sediment. Res.* **2015**, *85*, 990–998. [CrossRef]
37. Yu, J.; Song, Y.; Shi, K. Depositional facies and sequence architecture of the Yijianfang Formation in the Shuntuoguole Low Uplift, Tarim Basin, NW China. *Geol. J.* **2022**, *57*, 1890–1912. [CrossRef]
38. Jiao, Y.; Li, X.; Wang, Z. Mixed-water dissolution intervals in the Yingshan Formation (Lower Ordovician) of the Tarim Basin: Implications for karst reservoir development. *J. Pet. Geol.* **2019**, *42*, 451–468.

39. Wang, Y.P.; Bao, Z.D.; Zhang, L.J. Diagenesis of microbial dolomite reservoirs in the second Member of Dengying Formation of Ediacaran in the Penglai area, Sichuan Basin: Insights into the formation and evolution of high-quality reservoirs. *J. Geomech.* **2024**, *30*, 579−594.
40. Jiang, G.; Christie-Blick, N.; Kaufman, A.J.; Banerjee, D.M.; Rai, V. Carbonate platform growth and cyclicity at a terminal Proterozoic passive margin, Infra Krol Formation and Krol Group, Lesser Himalaya, India. *Sedimentology* **2003**, *50*, 921–952. [CrossRef]
41. James, N.P.; Choquette, P.W. *Paleokarst*; Springer: Berlin/Heidelberg, Germany, 1988; p. 416.
42. Shi, P.Z.; Li, T.; Zhu, Y.F.; Xie, Z.; Fan, K.Y. Geochemical characteristics and environmental implications of fracture-cave fillings: A case study of the Middle Ordovician Yijianfang Formation in Fuman Area, Tarim Basin. *Sci. Technol. Eng.* **2023**, *23*, 4527–4535. (In Chinese)

Disclaimer/Publisher's Note: The statements, opinions and data contained in all publications are solely those of the individual author(s) and contributor(s) and not of MDPI and/or the editor(s). MDPI and/or the editor(s) disclaim responsibility for any injury to people or property resulting from any ideas, methods, instructions or products referred to in the content.